Imaging of transparent spheres through a planar interface using a high-numerical-aperture optical microscope

Ben Ovryn

National Center for Microgravity Research for Fluids and Combustion, NASA–Glenn Research Center, MS 110-3, 21000 Brookpark Road, Cleveland, Ohio 44135, and Department of Mechanical and Aerospace Engineering, Case Western Reserve University, 10900 Euclid Avenue, Cleveland, Ohio 44106

Steven H. Izen

Department of Mathematics, Case Western Reserve University, 10900 Euclid Avenue, Cleveland, Ohio 44106

Received September 27, 1999; accepted February 28, 2000

The details of a model used to predict the scattering of a plane polarized wave by a spherical particle as observed with a microscope are presented. The model accounts for the effect of a refractive interface on the outgoing scattered field and determines the image produced by a lens with high numerical aperture. The predictions of the model are verified by direct comparison with the experimentally observed scattering from polystyrene spheres in a fluid. © 2000 Optical Society of America [S0740-3232(00)02207-9]

OCIS codes: 120.5820, 290.4020, 180.6900, 110.4100.

1. INTRODUCTION

In spite of the impressive gains in understanding the details of image formation in high-numerical-aperture (high-NA) conventional and confocal optical microscopes with point objects and planar reflectors,[1–3] the imaging of spherical objects is still a topic of intense theoretical and experimental interest. One way to gauge the difficulty in developing a complete, vector model that describes image formation for general three-dimensional objects is to realize that recently developed models describing the axial resolution[4] and the polarization sensitivity[5] of both confocal and conventional microscopes are based on either planar or point objects.

Understanding the complexities of image formation with spherical objects would be particularly significant for the following reasons: Scientists routinely track the movement of spherical tracer particles to help elucidate the behavior of complex systems,[6,7] and nearly spherical objects, such as red blood cells[8] and aerosol droplets,[9,10] are ubiquitous.

Attempts to model image formation with high-NA optical microscopes with arbitrary spherical objects have often required simplifying assumptions. For example, Weise *et al.*[11] recently presented a model to describe the image formed in a reflection confocal microscope; in addition to assuming that the sphere was perfectly reflecting, they used far-field calculations and limited the analysis to scalar predictions. Nevertheless, they showed good agreement with an experimental observation using a glass sphere glued to a microscope slide. It has been noted, however, that the optical imaging at high NA of real (e.g., biological) samples is seldom ideal, and therefore experimental observations are required to characterize the three-dimensional image formation.[12]

In this paper we examine the image of a spherical particle, illuminated by a plane wave, which moves in a fluid medium through the fixed focus of a conventional optical microscope. We refer to this as an "image"; however, our model predicts the scattering pattern that would be observed with an array detector in the image plane of the microscope and includes the effects of the optical system and the interface upon the propagation of the scattered wave front from the spherical particle. Although authors have modeled the effect of a high-NA lens on a converging electromagnetic wave[13–15] and they have examined the effect of an interface between the lens and the focus, these results are not directly applicable to the prediction of the image formed in a transmitted-light conventional microscope. To verify the scalar aspects of our model, we measured the scattering from spherical polystyrene particles in a fluid and directly compared it with model predictions. We have also used the model to predict the location of a particle in a three-dimensional flow in order to determine all three components of the fluid velocity.[16]

2. OPTICAL MODEL

The optical model that predicts the characteristics of the image can be separated into a sequence of elements. These elements include scattering from a spherical particle, refraction at a fluid–air interface, collection with a high-NA lens, and diffraction from the lens to the image plane.

Figure 1 represents schematically the experimental geometry. A spherical particle of radius a and index of refraction n_p is immersed in a fluid of index of refraction n_f, which is contained between two glass walls. The model assumes that the focus of the optical system is fixed and that the particle's location along the optical axis may change. We further assume that the fluid and the glass are index matched so effectively that there is a single interface with refractive index n_f, and therefore we refer to this as the interface. The scattered light is collected with a high-NA objective lens, and the intensity is measured at the image plane. In essence, we successively compute the electric and magnetic fields over four key xy planes, which are perpendicular to the optical (z) axis. The model has the following six elements, each of which is discussed in detail in Subsections 2.A–2.F:

1. Evaluate the scattered electric and magnetic fields at the fluid side of the interface (plane 1^-). These are the fields scattered by the spherical particle.
2. Calculate the transmission of the scattered fields to the air side of the interface (plane 1^+).
3. Propagate the scattered fields from the interface to the entrance pupil (plane 2) of the objective lens.
4. Without adopting a paraxial approximation, calculate the polarization rotation, the phase transformation, and the scaling of the scattered fields from the entrance pupil to the exit pupil (plane 3) of the lens.
5. Propagate the incident electromagnetic fields to the exit pupil (plane 3) of the lens.
6. Calculate the diffraction of the superposed incident and scattered fields (the total field) from the exit pupil to the image plane (plane 4). Compute the irradiance at the image plane.

A. Scattered Field at the Interface

In this subsection we review some salient features of the scattering of electromagnetic plane waves from arbitrary-size, homogeneous spheres in a medium with arbitrary but homogeneous index of refraction. The Cartesian coordinate system, with positive z directed along the optical axis from the particle to the image, is centered at the scattering sphere (Fig. 2).

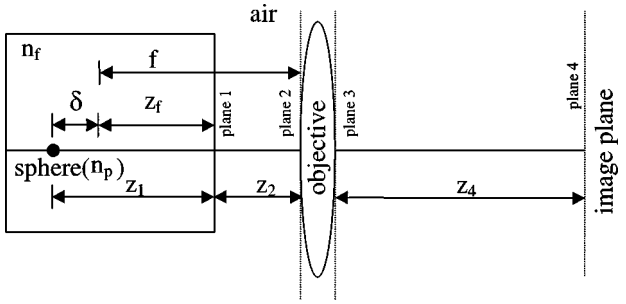

Fig. 1. Schematic representing the model geometry. A particle, with index of refraction n_p and radius a, is in a fluid medium with index n_f. The particle's position along the optical axis may change by an amount δ with respect to a reference distance z_1 from the fluid–air interface. The quantities z_1 and z_2 are determined from the experimental parameters by using $z_1 = z_f + \delta$ and $z_2 = f - z_f/n_f$, where z_f is measured, f is the focal length, and positive δ indicates a greater distance from plane 1. The electromagnetic fields are successively computed over the four labeled planes.

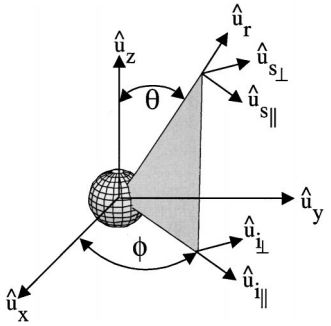

Fig. 2. Geometry of the basis vectors $\hat{\mathbf{u}}_{s\parallel}$, $\hat{\mathbf{u}}_{s\perp}$, $\hat{\mathbf{u}}_{sr}$, $\hat{\mathbf{u}}_{i\parallel}$, and $\hat{\mathbf{u}}_{i\perp}$.

All the electromagnetic fields are assumed to be time harmonic, of the form

$$\mathbf{E}(\mathbf{x}, t) = \mathrm{Re}[\mathbf{E}(\mathbf{x})\exp(-i\omega t)]. \tag{1}$$

$\mathbf{E}(\mathbf{x})$ is a transverse solution to the vector Helmholtz equation $\nabla^2\mathbf{E} + k\mathbf{E} = \mathbf{0}$. Corresponding to each given expression for the electric field $\mathbf{E}$ is a similar expression for the magnetic field $\mathbf{H}$. The wave vector is denoted by $\mathbf{k}$, and $k = \|\mathbf{k}\| = 2\pi/\lambda$ is the wave number, with λ as the wavelength in the medium.

The incident illumination $\mathbf{E}_i$ is assumed to be a monochromatic spatially coherent linearly polarized plane wave traveling along the (positive z) direction of the optical axis. Without loss of generality, we take the polarization along the x axis. Therefore

$$\mathbf{E}_i = E_0\hat{\mathbf{u}}_x \exp ikz, \tag{2}$$

where $\hat{\mathbf{u}}_x$ is the unit vector in the x direction.

The incident illumination is scattered by a sphere of radius a and index of refraction n_p surrounded by a medium of index of refraction n_f. An analytic expression for the scattering in this geometry (given by the solution to the vector Helmholtz equation with appropriate boundary conditions) was given by Mie in 1908.[17–19]

The total field $\mathbf{E}$ external to the particle is a superposition of the incident and scattered fields:

$$\mathbf{E} = \mathbf{E}_i + \mathbf{E}_s. \tag{3}$$

The incident field $\mathbf{E}_i$ can be written in terms of components in the directions $\hat{\mathbf{u}}_{i\parallel}$ and $\hat{\mathbf{u}}_{i\perp}$ with respect to the scattering plane. With (r, θ, ϕ) as the standard spherical coordinate representation for (x, y, z), the basis vectors $\hat{\mathbf{u}}_{i\parallel}$ and $\hat{\mathbf{u}}_{i\perp}$ exhibit ϕ dependence (Fig. 2):

$$\hat{\mathbf{u}}_{i\parallel}(\phi) = \cos\phi\,\hat{\mathbf{u}}_x + \sin\phi\,\hat{\mathbf{u}}_y, \tag{4a}$$

$$\hat{\mathbf{u}}_{i\perp}(\phi) = -\sin\phi\,\hat{\mathbf{u}}_x + \cos\phi\,\hat{\mathbf{u}}_y. \tag{4b}$$

The incident field is

$$\mathbf{E}_i = (\exp ikz)[(E_0\cos\phi)\hat{\mathbf{u}}_{i\parallel}(\phi) - (E_0\sin\phi)\hat{\mathbf{u}}_{i\perp}(\phi)]$$
$$\equiv (\exp ikz)[E_{i\parallel}(\phi)\hat{\mathbf{u}}_{i\parallel}(\phi) + E_{i\perp}(\phi)\hat{\mathbf{u}}_{i\perp}(\phi)]. \tag{5}$$

For the scattered field (Fig. 2), the basis set is

$$\hat{\mathbf{u}}_{s\parallel}(\theta, \phi) \equiv \hat{\mathbf{u}}_\theta = \cos\theta\cos\phi\hat{\mathbf{u}}_x + \cos\theta\sin\phi\,\hat{\mathbf{u}}_y - \sin\theta\,\hat{\mathbf{u}}_z, \tag{6a}$$

$$\hat{\mathbf{u}}_{s\perp}(\phi) \equiv \hat{\mathbf{u}}_{\phi} = -\sin\phi\,\hat{\mathbf{u}}_x + \cos\phi\,\hat{\mathbf{u}}_y, \tag{6b}$$

$$\hat{\mathbf{u}}_{sr}(\theta, \phi) \equiv \hat{\mathbf{u}}_r = \sin\theta\cos\phi\,\hat{\mathbf{u}}_x + \sin\theta\sin\phi\,\hat{\mathbf{u}}_y + \cos\theta\,\hat{\mathbf{u}}_z, \tag{6c}$$

where $\hat{\mathbf{u}}_\theta$, $\hat{\mathbf{u}}_\phi$, and $\hat{\mathbf{u}}_r$ are the standard unit vectors in spherical coordinates. The field scattered from the particle becomes

$$\mathbf{E}_s(r, \theta, \phi) = E_{s\parallel}(r, \theta, \phi)\hat{\mathbf{u}}_{s\parallel}(\theta, \phi) + E_{s\perp}(r, \theta, \phi)\hat{\mathbf{u}}_{s\perp}(\phi) + E_{sr}(r, \theta, \phi)\hat{\mathbf{u}}_{sr}(\theta, \phi). \tag{7}$$

A representation of $\mathbf{E}_s(r, \theta, \phi)$ in terms of vector spherical harmonics is presented in Appendix A. In Appendix B the asymptotic values of the harmonic functions are evaluated to determine the accuracy of the commonly employed far-field approximations. As shown in Appendix B, the radial component of the scattered electric field is less than 1% of the transverse components and may be dropped without incurring a significant error. Equivalently, the transverse components of the Poynting vector are small compared with the radial component, so effectively, $\mathbf{E}_s$ propagates radially. Therefore $\mathbf{E}_s$ reduces to

$$\mathbf{E}_s(r, \theta, \phi) = E_{s\parallel}(r, \theta, \phi)\hat{\mathbf{u}}_{s\parallel}(\theta, \phi) + E_{s\perp}(r, \theta, \phi)\hat{\mathbf{u}}_{s\perp}(\phi). \tag{8}$$

The coefficients $E_{s\parallel}(r, \theta, \phi)$ and $E_{s\perp}(r, \theta, \phi)$ are given by

$$E_{s\parallel}(r, \theta, \phi) = S_{\parallel}(r, \theta)E_{i\parallel}(\phi), \tag{9a}$$

$$E_{s\perp}(r, \theta, \phi) = S_{\perp}(r, \theta)E_{i\perp}(\phi), \tag{9b}$$

where $S_{\parallel}(r, \theta)$ and $S_{\perp}(r, \theta)$ are the elements of the *near-field* scattering amplitude matrix. Note that the near-field scattering amplitudes must be used because a far-field approximation yields an error as large as 7% (Appendix B). In essence, the interface, at a distance z_1 from the particle, is far enough away from the particle such that the radial component has decayed enough to be neglected, but it is not far enough away for the substitution of $(-i)^n(\exp ikr)/ikr$ for the spherical Hankel function $h_n^{(1)}(kr)$ to be valid.

B. Effect of the Interface

In the absence of the interface between the spherical particle and the lens, the appropriate approach to determining the fields over the entrance pupil would be to evaluate the Mie field directly on the entrance pupil.[9] Because of the interface, however, we must account for refraction. We adopt a ray approach to propagate the field from the interface to the entrance pupil.

The ray approach is justified because the scattered electric and magnetic fields behave asymptotically like outgoing spherical waves with angular dependence.[17] Because the entrance pupil is in the far zone, the arguments in Section 3.2.2 of Ref. 20 imply that only one plane wave of the angular spectrum representation will contribute to the asymptotic behavior of the field at a particular point on the entrance pupil. We assume that Fresnel formulas are applicable to each plane-wave component at the interface. This approach also accounts for the polarization rotation of the refracted ray, preserving the vectorial nature of the field.[21]

As indicated in the subsection on numerical implementation (Subsection 2.G), the location of the discrete rays used to propagate the scattered field to the entrance pupil of the lens is ultimately governed by the grid used at the exit pupil for the numerical evaluation of the highly oscillatory Fresnel diffraction integral. In turn, the grid on the exit pupil is related to the grid on the image plane that corresponds to the pixels in the array detector. The determination of the field over these key planes will be provided in subsequent subsections.

Figure 3 shows the effect of refraction on a ray centered on the particle. The propagating scattered field encounters the interface (plane 1). Polar coordinates on this plane are denoted by ρ_1 and ϕ, where

$$\rho_1 = z_1 \tan\theta, \tag{10}$$

with z_1 denoting the distance from the particle center to the interface. With this notation the scattered field $\mathbf{E}_{s1^-}$ on the fluid side of the interface may be expressed as

$$\mathbf{E}_{s1^-}(\rho_1, \phi) = \mathbf{E}_s(\sqrt{\rho_1^2 + z_1^2}, \tan^{-1}(\rho_1/z_1), \phi). \tag{11}$$

At the interface the scattered field is refracted and propagates in a new direction β, which is given by Snell's law:

$$n_f \sin\theta = \sin\beta. \tag{12}$$

On the air side of the interface, the scattered field $\mathbf{E}_{s1^+}$ may be expressed as

$$\mathbf{E}_{s1^+}(\rho_1, \phi) = E_{s\parallel 1^+}(\rho_1, \phi)\hat{\mathbf{u}}_{s\parallel}(\beta, \phi) + E_{s\perp 1^+}(\rho_1, \phi)\hat{\mathbf{u}}_{s\perp}(\phi). \tag{13}$$

With the use of Eqs. (9), the coefficients $E_{s\parallel 1^+}(\rho_1, \phi)$ and $E_{s\perp 1^+}(\rho_1, \phi)$ are given by

$$E_{s\parallel 1^+}(\rho_1, \phi) = t_{\parallel}E_{s\parallel 1^-}(\rho_1, \phi) = t_{\parallel}S_{\parallel}E_{i\parallel}(\phi), \tag{14a}$$

$$E_{s\perp 1^+}(\rho_1, \phi) = t_{\perp}E_{s\perp 1^-}(\rho_1, \phi) = t_{\perp}S_{\perp}E_{i\perp}(\phi), \tag{14b}$$

where $t_{\parallel}$ and $t_{\perp}$ are the Fresnel coefficients for the transmitted field at the interface[21]:

$$t_{\parallel} = \frac{2\cos\theta n_f}{\cos\beta + n_f\cos\theta}, \tag{15a}$$

$$t_{\perp} = \frac{2\cos\theta n_f}{\cos\theta + n_f\cos\beta}. \tag{15b}$$

Upon refraction at the interface, the parallel component of the scattered field has rotated from the $\hat{\mathbf{u}}_{s\parallel}(\theta, \phi)$ direction to the $\hat{\mathbf{u}}_{s\parallel}(\beta, \phi)$ direction, but the direction of the perpendicular component remains unchanged. The ampli-

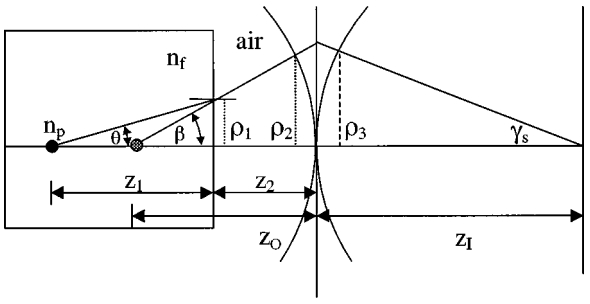

Fig. 3. Geometry of the fluid–air interface and the parameters that govern the lens transformation.

tudes of the transverse magnetic and transverse electric components $E_{s\|1}(\rho_1, \phi)$ and $E_{s\perp 1}(\rho_1, \phi)$ are given with respect to the plane of the interface.

C. Scattered Field at the Entrance Pupil of the Lens

To determine the relationship between the field $\mathbf{E}_{s2}$ at the entrance pupil and the field at the interface, we account for the change in phase along each ray as it propagates in free space from (ρ_1, ϕ) on the interface to (ρ_2, ϕ) on the entrance pupil and account for changes in magnification. Because the fields to be propagated are not yet in the far zone (see the end of Subsection 2A and Appendix B), the change in phase is not strictly linear with respect to distance. Numerical computations, however, reveal that treating the phase change as linear introduces an error in the fields on the order of 0.1%.

The radial distance ρ_2 on the entrance pupil is given by (Fig. 3)

$$\rho_2 = z_1 \tan\theta + z_2 \tan\beta. \tag{16}$$

The magnification $m(\theta, \beta)$ of the bundle of rays with the use of Eqs. (10), (12), and (16) with fixed z_1 and z_2 can be expressed in terms of θ and β as

$$m(\theta, \beta) = \frac{d\rho_2}{d\rho_1} = 1 + n_f \frac{z_2 \cos^3\theta}{z_1 \cos^3\beta}. \tag{17}$$

By analogy with the scattered field on the interface, the field at the entrance pupil is

$$\mathbf{E}_{s2}(\rho_2, \phi) = E_{s\|2}(\rho_2, \phi)\hat{\mathbf{u}}_{s\|}(\beta, \phi) + E_{s\perp 2}(\rho_2, \phi)\hat{\mathbf{u}}_{s\perp}(\phi), \tag{18a}$$

where the coefficients $E_{s\|2}(\rho_2, \phi)$ and $E_{s\perp}(\rho_2, \phi)$ are given by

$$E_{s\|2}(\rho_2, \phi) = \psi_{s12} E_{s\|1^+} = \psi_{s12} t_\| S_\| E_{i\|}(\phi), \tag{18b}$$

$$E_{s\perp 2}(\rho_2, \phi) = \psi_{s12} E_{s\perp 1^+} = \psi_{s12} t_\perp S_\perp E_{i\perp}(\phi), \tag{18c}$$

with

$$\psi_{s12} = \frac{1}{m(\theta, \beta)} (\exp ik_0)[(\rho_2 - \rho_1)^2 + {z_2}^2]^{1/2}, \tag{18d}$$

where k_0 is the free-space wave number.

D. Scattered Field at the Exit Pupil of the Lens

In a high-NA lens, the precise transformation of the field from the entrance pupil to the exit pupil requires a detailed model of the lens, which is generally unavailable. Therefore simplifying assumptions must be made about the behavior of the lens.[22] We will proceed by making the assumption that the imaging lens in our model transforms a diverging spherical wave with radius of curvature z_O at the entrance pupil into a converging spherical wave with radius of curvature z_I. Also, we model the lens as diffraction limited and aplanatic. Therefore the lens imparts a phase transformation, a scaling, and a rotation of polarization.[23]

To determine the effect of the lens, we construe each ray at the entrance pupil as being part of a diverging spherical wave with a radius of curvature determined by the angle β of the ray with respect to the optical axis. The effective radius of curvature at the entrance pupil is the quantity $z_O = \rho_2 \tan\beta$ (Fig. 3). The variation of the radius of curvature with the distance ρ_2 is a consequence of the spherical aberration introduced by the interface; in the absence of the interface, the radius of curvature would be constant at all points on the entrance pupil. The effective radius of curvature of the corresponding ray leaving the exit pupil, z_I, is given by the lens formula

$$z_I = \frac{z_O f}{z_O - f}, \tag{19}$$

where f is the focal length of the lens. Using Abbe's sine condition,[21] we obtain

$$z_I \sin\gamma_s = z_O \sin\beta, \tag{20}$$

where γ_s is the angle at which the ray leaving the exit pupil approaches the geometrical focus (Fig. 3). A ray entering the lens at a distance from the optical axis of ρ_2 will exit at ρ_3, where

$$\rho_3 = \frac{\cos\beta}{\cos\gamma_s} \rho_2. \tag{21}$$

The scaling for the field amplitude of the aplanatic lens is[24] $(\cos\gamma_s/\cos\beta)^{1/2}$.

The polarization rotation upon passage through the lens is analogous to that which occurred at the interface. The parallel component of the scattered field will be rotated from the $\hat{\mathbf{u}}_{s\|}(\beta, \phi)$ direction to the $\hat{\mathbf{u}}_{s\|}(\pi - \gamma_s, \phi)$ direction, but the direction of the perpendicular component remains unchanged. The angle $\pi - \gamma_s$ has been used because γ_s is measured with respect to the $-\hat{\mathbf{u}}_z$ direction (Fig. 3).

Therefore the scattered field on the exit pupil becomes

$$\mathbf{E}_{s3}(\rho_3, \phi) = E_{s\|3}(\rho_3, \phi)\hat{\mathbf{u}}_{s\|}(\pi - \gamma_s, \phi) + E_{s\perp 3}(\rho_3, \phi)\hat{\mathbf{u}}_{s\perp}(\phi), \tag{22a}$$

where the coefficients $E_{s\|3}(\rho_3, \phi)$ and $E_{s\perp 3}(\rho_3, \phi)$ are given by

$$E_{s\|3}(\rho_3, \phi) = \psi_{s23} E_{s\|2}(\rho_2, \phi) = \psi_{s23}\psi_{s12} t_\| S_\| E_{i\|}(\phi), \tag{22b}$$

$$E_{s\perp 3}(\rho_3, \phi) = \psi_{s23} E_{s\perp 2}(\rho_2, \phi) = \psi_{s23}\psi_{s12} t_\perp S_\perp E_{i\perp}(\phi), \tag{22c}$$

with

$$\psi_{s23} = \left(\frac{\cos\gamma_s}{\cos\beta}\right)^{1/2} \exp ik_0[z_O - ({\rho_2}^2 + {z_O}^2)^{1/2}] \times \exp ik_0[z_I - ({\rho_3}^2 + {z_I}^2)^{1/2}]. \tag{22d}$$

The two phase factors represent the incremental phase from the object and image sides of the lens, respectively.[25] If necessary, the effect of lens aberrations could be modeled as an additional phase factor.

E. Incident Field at the Exit Pupil of the Lens

The propagation of the incident field $\mathbf{E}_i$ to the exit pupil is computed by a method similar to that of propagation of the scattered field $\mathbf{E}_s$. Because the incident illumination is planar and polarized perpendicularly to the optical axis, the direction of propagation before the lens is restricted to the optical axis and the algebra is simplified.

The incident electric field $\mathbf{E}_{i1^-}$ at the fluid side of the interface (Fig. 4) is

$$\mathbf{E}_{i1^-} = E_0 \psi_{i01} \hat{\mathbf{u}}_x , \tag{23a}$$

where

$$\psi_{i01} = \exp ikz_1 . \tag{23b}$$

On the air side of the interface, the incident field becomes

$$\mathbf{E}_{i1^+} = t\mathbf{E}_{i1^-} = E_0 t \psi_{i01} \hat{\mathbf{u}}_x , \tag{24a}$$

where t is the Fresnel coefficient[21]

$$t = \frac{2n_f}{1 + n_f}. \tag{24b}$$

The field $\mathbf{E}_{i1^+}$ will propagate the distance z_2 (in air) to the entrance pupil and accumulate an additional phase term. At the entrance pupil, the field becomes

$$\mathbf{E}_{i2} = \psi_{i12}\mathbf{E}_{i1^+} = E_0 \psi_{i12} t \psi_{i01} \hat{\mathbf{u}}_x , \tag{25a}$$

where

$$\psi_{i12} = \exp ik_0 z_2 . \tag{25b}$$

Expressed in terms of $\hat{\mathbf{u}}_{i\|}(\phi)$ and $\hat{\mathbf{u}}_{i\perp}(\phi)$, $\mathbf{E}_{i2}$ becomes

$$\mathbf{E}_{i2}(\rho_2, \phi) = E_{i\|2}(\phi)\hat{\mathbf{u}}_{i\|}(\phi) + E_{i\perp 2}(\phi)\hat{\mathbf{u}}_{i\perp}(\phi), \tag{26a}$$

where the coefficients $E_{i\|2}(\phi)$ and $E_{i\perp 2}(\phi)$ are

$$E_{i\|2}(\phi) = \psi_{i12} t \psi_{i01} E_{i\|}(\phi), \tag{26b}$$

$$E_{i\perp 2}(\phi) = \psi_{i12} t \psi_{i01} E_{i\perp}(\phi). \tag{26c}$$

After passing through the lens, the plane wave becomes a converging spherical wave with radius f. By analogy with the scattered wave, there is a phase transformation, a scaling, and a polarization rotation. The transformation of the plane wave is a limiting case of Eqs. (22), with $\cos\beta = 1$. In this limit, the ray leaving the exit pupil at (ρ_3, ϕ) makes an angle of γ_i with the optical axis:

$$\gamma_i = \sin^{-1}(\rho_3/f). \tag{27}$$

The polarization rotation of the parallel component of the incident wave upon passage through the lens is given by replacing $\hat{\mathbf{u}}_{i\|}(\phi)$ with $\hat{\mathbf{u}}_{s\|}(\pi - \gamma_i, \phi)$. As above, the perpendicular component remains unchanged. From Eqs. (4b), (6b), and (6c), $\hat{\mathbf{u}}_{i\perp}(\phi)$ is identical to $\hat{\mathbf{u}}_{s\perp}(\phi)$. Thus, after propagation to the exit pupil, the incident field $\mathbf{E}_{i3}$ is

$$\mathbf{E}_{i3}(\rho_3, \phi) = E_{i\|3}(\rho_3, \phi)\hat{\mathbf{u}}_{s\|}(\pi - \gamma_i, \phi) + E_{i\perp 3}(\rho_3, \phi)\hat{\mathbf{u}}_{s\perp}(\phi), \tag{28a}$$

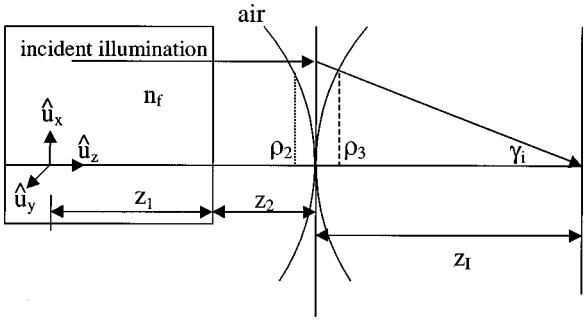

Fig. 4. Propagation of the incident field to the image plane.

where the coefficients $E_{i\|3}(\rho_3, \phi)$ and $E_{i\perp 3}(\rho_3, \phi)$ are given by

$$E_{i\|3}(\rho_3, \phi) = \psi_{i23}E_{i\|2}(\phi) = \psi_{i23}\psi_{i12}t\psi_{i01}E_{i\|}(\phi), \tag{28b}$$

$$E_{i\perp 3}(\rho_3, \phi) = \psi_{i23}E_{i\perp 2}(\phi) = \psi_{i23}\psi_{i12}t\psi_{i01}E_{i\perp}(\phi), \tag{28c}$$

with

$$\psi_{i23} = \sqrt{\cos\gamma_i}\exp ik_0[f - (\rho_3{}^2 + f^2)^{1/2}]. \tag{28d}$$

F. Determination of the Field at the Image Plane

A two-dimensional diffraction calculation is used to propagate the total field $\mathbf{E}_3$ (the superposition of the incident and scattered fields) from the exit pupil to the detector plane:

$$\mathbf{E}_3(\rho_3, \phi) = \mathbf{E}_{s3}(\rho_3, \phi) + \mathbf{E}_{i3}(\rho_3, \phi) \tag{29a}$$

$$= E_{i\|3}(\rho_3, \phi)\hat{\mathbf{u}}_{s\|}(\pi - \gamma_i, \phi) + E_{s\|3}(\rho_3, \phi)\hat{\mathbf{u}}_{s\|}(\pi - \gamma_s, \phi) + [E_{i\perp 3}(\rho_3, \phi) + E_{s\perp 3}(\rho_3, \phi)]\hat{\mathbf{u}}_{s\perp}(\phi). \tag{29b}$$

To determine the irradiance distribution at a planar detector that is normal to the optical axis and located at a distance z_4 from the exit pupil, we must compute a vector diffraction integral over the exit pupil. This diffraction integral may be simplified by using a vector Kirchhoff approximation. That is, each Cartesian component of the field is individually subjected to a scalar diffraction calculation. With an inconsequential constant phase factor omitted, the field on the image plane is given by the Fresnel integral[25]

$$\mathbf{E}_4(\rho_4, \alpha) = \frac{1}{\lambda z_4}\exp\left(\frac{\pi i}{\lambda z_4}\rho_4{}^2\right) \times \int_0^A \int_0^{2\pi} W_\mu(\rho_3)\mathbf{E}_3(\rho_3, \phi)\exp\left(\frac{\pi i}{\lambda z_4}\rho_3{}^2\right) \times \exp\left[\frac{-\pi i}{\lambda z_4}\rho_4\rho_3\cos(\phi - \alpha)\right]\rho_3 \mathrm{d}\phi \mathrm{d}\rho_3 , \tag{30}$$

where A is the radius of the exit pupil and (ρ_4, α) are polar coordinates on the image plane. Equation (30) also contains a windowing function $W_\mu(\rho_3)$ to attenuate Gibbs ringing from the edge of the lens:

$$W_\mu(\rho_3) = \begin{cases} 1 & \rho_3 \leq \mu A \\ \frac{1}{2}\left[1 + \cos\frac{(\rho_3 - \mu A)\pi}{(1 - \mu)A}\right] & \mu A < \rho_3 \leq A \end{cases}. \tag{31}$$

As shown in Appendix C [Eq. (C10)], the normalized irradiance on the image plane determined from the Poynting vector is

$$I(\rho_4, \alpha) = |E_4^0(\rho_4)|^2 + |E_4^2(\rho_4)|^2 + 2\,\mathrm{Re}\{E_4^0(\rho_4)[E_4^2(\rho_4)]^*\cos 2\alpha\}, \tag{32}$$

where the coefficients E_4^0 and E_4^2 are given in Eqs. (C7). Equation (32) represents the transformation of the x-polarized incident field by all of the elements of our model. If the incident illumination is an unpolarized plane wave, then the irradiance on the detector may be determined from Eqs. (C7):

$$I_{\text{unpolarized}}(\rho_4) = \frac{1}{2\pi}\int_0^{2\pi} I(\rho_4, \alpha)\mathrm{d}\alpha = |E_4^0(\rho_4)|^2 + |E_4^2(\rho_4)|^2. \quad (33)$$

G. Numerical Implementation

In this subsection we discuss the issues that arise in the numerical computation of the irradiance $I(\rho_4, \alpha)$. The three integrals in Eq. (C7b) have integrands that are highly oscillatory, and special attention must be paid to ensure that the integral is computed accurately.[26] To avoid a loss of precision, one must make the grid at the exit pupil dense enough to sample even the most highly oscillatory regions. Because this region and the maximum frequency of oscillation depends on the value of ρ_4 at which these integrals are being evaluated, an efficient method would be to use an adaptive sampling algorithm. Instead, a simpler, regular sampling of ρ_3 was chosen to be dense enough to handle the highest oscillations that can appear for any value of ρ_4. The penalty for this simpler approach is slower execution times.

For each sample point ρ_3 on the exit pupil, the quantities $E_3^0(\rho_3)$ and $E_3^2(\rho_3)$ given in Eqs. (C5) must be evaluated. To compute the contribution from the incident wave, we must compute γ. With the use of Eqs. (27) and (28), $\mathbf{E}_{i3}(\rho_3)$ is immediately available. The computation of $\mathbf{E}_{s3}(\rho_3)$ is more involved. The sample point ρ_3 determines the ray required to propagate the scattered field through the optical system. This computation requires knowledge of the quantities ρ_2, ρ_1, γ_s, β, and θ, which are used to locate the ray. Equations (10), (12), (16), and (21) uniquely determine all of these quantities. Although it is possible to write down analytic expressions for these variables in terms of ρ_3, such expressions are complicated. Instead, an iterative procedure has been adopted to numerically determine values for ρ_2, ρ_1, γ_s, β, and θ consistent with the sample point ρ_3. After these variables have been determined, the scattered fields can be propagated to the exit pupil by using Eqs. (9), (14), (18), and (22).

H. Summary of the Algorithm

Before comparing the numerical results with the observed scattering, we briefly reiterate the algorithm.

1. Input the physical parameters describing the optical properties and the geometry (these parameters will be discussed in Section 3).
2. Choose a regular grid on the exit pupil dense enough to accurately perform the diffraction integrals.
3. For each grid point on the exit pupil, iteratively determine the quantities ρ_2, ρ_1, γ_s, and β, thereby determining the grid points on the entrance pupil and on the interface.
4. Compute the scattered fields on the fluid side of the interface by using Mie's formulas.
5. Propagate the scattered fields from the interface to the exit pupil.
6. Sum the incident and scattered fields at the exit pupil and numerically evaluate the diffraction integrals. Compute the irradiance at each pixel in the detector array.

3. EXPERIMENTAL METHOD

To test the model, we measured the scattering from a spherical particle in a fluid medium at several distances along the optical axis and compared it with numerical calculations. Spherical polystyrene particles (Duke Scientific Corp., catalog #252) with radius $a = 3.5 \pm 0.1\,\mu$m, index of refraction $n_p = 1.5847$, and density $\rho = 1.05\,\text{g/cm}^3$ were contained in a thin channel. The channel was formed from two 1.25-mm glass slides held in a frame that had a machined spacer on the periphery; the dimensions of the resulting chamber were 6 mm $\times$ 48 mm $\times$ 0.315 mm. The channel was filled from one side through an inlet (a reservoir was connected on the exit end) with immersion liquid (Cargille, Inc., index of refraction $n_f = 1.495$, density $\rho \approx 0.88\,\text{g/cm}^3$, and viscosity $\mu \approx 27$ cps); there was no transverse flow (and therefore no bulk transverse motion of the particle) when the inlet and exit values were closed. The sample chamber was placed horizontally on a translation stage of a transmitted-light microscope (Zeiss, Jenapol Interphako) equipped with a 25×/0.5-NA infinity-corrected, planachromat objective with an 11-mm working distance. The objective was used with the manufacturer-supplied compensator for a 2-mm cover slide. The illuminating wave front was produced by using the microscope's Köhler source with a notch filter; the condenser aperture was set to 2 mm. The measured center wavelength for the filter was $\lambda = 525$ nm with a full width at half-maximum of 85 nm. A high-density, digital CCD array (Photometrics PXL 1400) with 1317 $\times$ 1035 pixels (each pixel is 6 μm$\times$ 6 μm with 100% fill factor) was mounted on the photography port of the microscope. To increase the magnification of the acquired image, we inserted a 10× eyepiece between the port and the CCD array. The dynamic range of the array was 12 bits, and it was cooled to −25 °C before acquiring images. A dark current image was obtained and subsequently subtracted from all of the images. The spatial resolution, determined by using an optical reference standard (Geller Microanalytical, Inc., MRS-3), was approximately 8.5 pixels/μm.

Measuring the scattering patterns was a two-step process. In the first step, a sphere was dislodged from the top glass slide by applying a brief shear; the shear was produced by opening the exit valve of the channel. After cessation of the shear, the particle was observed to have negligible transverse velocity, and it began to fall downward (toward the illumination source). The particle's settling velocity was determined by measuring the change in focus (at 1-min intervals) required to maintain a fixed scattering pattern (nominally Gaussian best focus).

In the second step, the focus of the microscope was kept fixed near the midpoint of the channel (approximately 150 μm from the fluid–air interface). Another particle was

similarly dislodged from the top slide, and its position along the optical axis varied because of settling. Eighty images of the scattering from this particle were then acquired at 15-s intervals without changing the focus of the microscope. An initial estimate of the particle's location along the optical axis for each of the 80 patterns was determined by using the estimate of the particle's velocity and initial position.

For a comparison of the numerical and experimental results, initial estimates for the experimental parameters were required. Although initial estimates for the parameters that govern the scattering were known to within experimental error, the absence of the complete design specifications for the objective lens required simplifying assumptions. For the Mie scattering calculations, the relative index of refraction between the particle and the fluid and the size parameter were taken to be $n = 1.06$ and $ka = 62.622$, respectively. The parameter z_1, which represents the $\delta = 0$ location of the numerical prediction, was estimated to be $z_1 = 1.4$ mm by adding the thickness of the front wall of the channel (1.25 mm) to the estimate of the focus position from the fluid–air interface (150 μm). To numerically determine the effect of the objective, we asked the manufacturer to supply the focal length of the objective and the distance from the tube lens to the intermediate image plane.[3] These values, 25.1 mm and 245 mm, respectively, were used to estimate the object (z_O) and image (z_I) distances, respectively. Additionally, the numerical aperture was used to estimate the size of the entrance pupil of the lens.

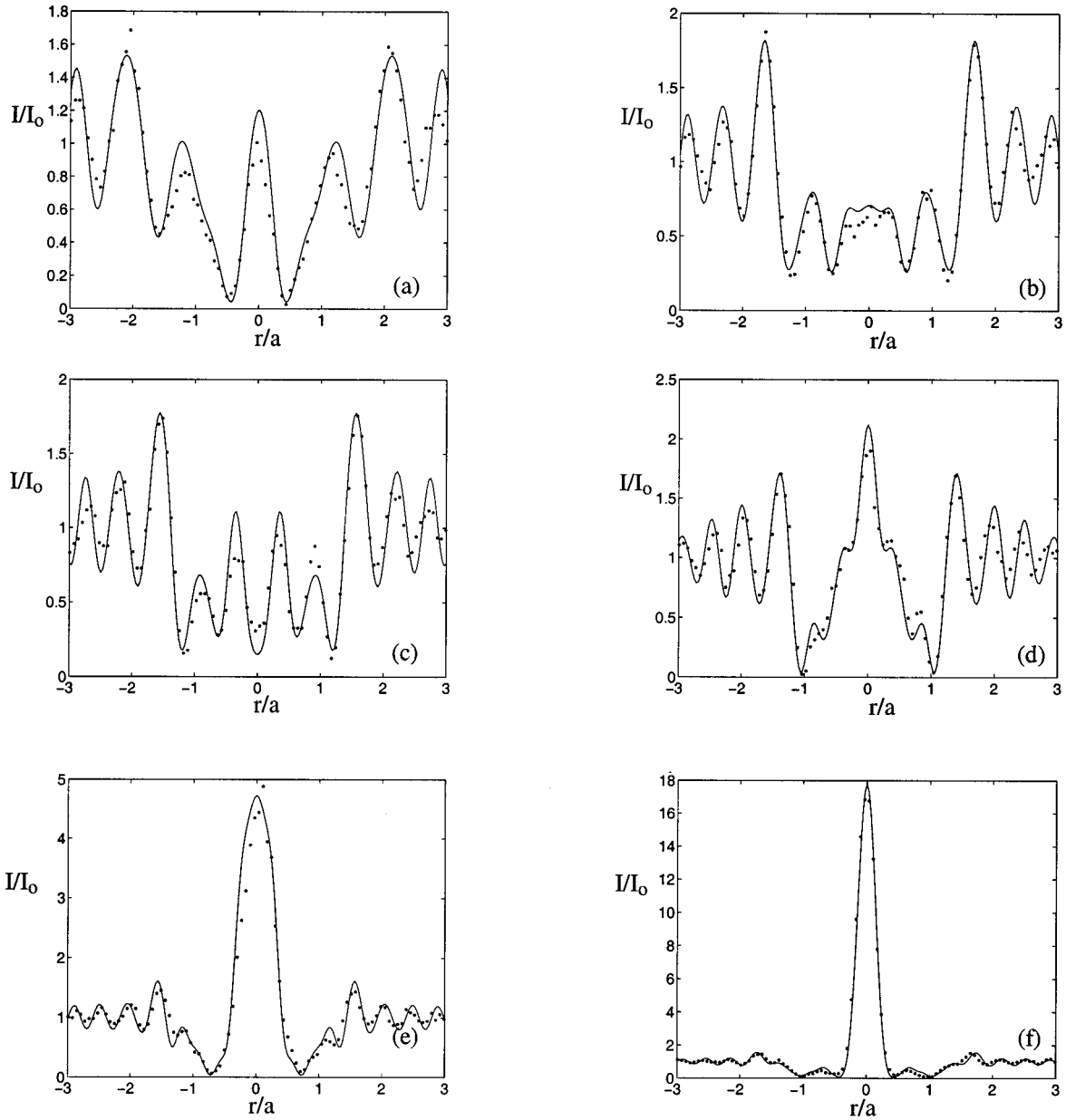

Fig. 5. Experimental and predicted scattering shown as a function of transverse distance on the detector plane at six values of δ: (a) -25.70 μm, (b) -6.10 μm, (c) -2.50 μm, (d) 4.00 μm, (e) $+14.9$ μm, (f) $+22.1$ μm.

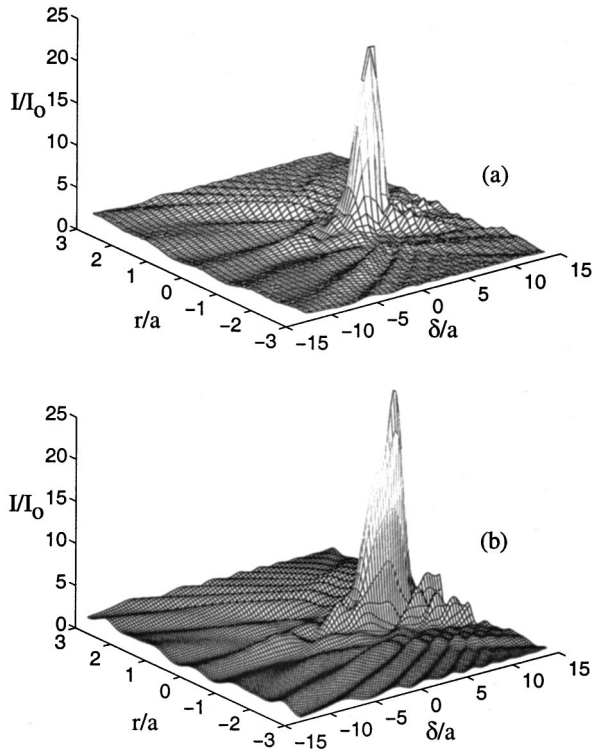

Fig. 6. (a) Experimental and (b) predicted scattering shown as a function of particle position along the optical axis and transverse distance on the detector plane.

4. RESULTS

The settling velocity of the particle, measured in the first step of the experimental procedure, $10.2 \pm 1.6\,\mu$m/min, agreed with the Stokes velocity, which was predicted from the sphere's radius and the density difference between the sphere and the fluid. With the use of this settling velocity, it was possible to obtain an initial estimate for the location of the sphere as a function of time.

Figure 5 shows both the measured and the predicted intensity from a single particle at six different locations. The solid curves are the numerically predicted scattering patterns. As shown in Fig. 1, a positive distance δ indicates that the particle is further from the objective lens. The axial distances δ were $-25.70\ \mu$m, $-6.10\ \mu$m, $-2.50\ \mu$m, $+4.00\ \mu$m, $+14.90\ \mu$m, and $+22.10\ \mu$m, for Figs. 5(a), 5(b), 5(c), 5(d), 5(e), and 5(f), respectively. The intensities are normalized with respect to the incident intensity (the intensity far from the center of the particle), and the transverse distances are normalized with respect to the particle radius. Figure 6 shows three-dimensional plots of (a) the experimental data and (b) the theoretical scattering patterns as a function of distance along the optical axis (δ/a). The experimental data contain 39 datasets, and the theoretical dataset contains 95 scattering calculations spaced at 1.0-μm intervals. To avoid an extremely dense plot, we display every other pixel in the transverse direction. The parameters used for the numerical calculations shown in Figs. 5 and 6 were $n_p = 1.585$, $n_f = 1.495$, $a = 3.65\,\mu$m, $\lambda = 510$ nm, and a distance $z_1 = 1.4$ mm. In addition, a trial-and-error approach was used to determine the best value for the parameter μ in Eq. (31); a value of 0.98 was used.

5. DISCUSSION

As indicated in Figs. 5 and 6, the model prediction shows good agreement with experimental data. To calculate the intensity for any value of δ, the model requires the following parameters as inputs: (1) the radius of the particle, (2) the refractive index of the particle, (3) the refractive index of the medium, (4) the wavelength of the illumination in the medium, (5) the distance of the particle to the fluid–air interface ($z_f + \delta$), (6) the focal length of the objective, (7) the distance from the tube lens to the intermediate image, and (8) the numerical aperture of the objective. To obtain the agreement between the measured and numerically calculated data, we had to adjust the values for the experimental parameters from their initial values. A possible explanation for the difference between the initial values and the best-fit size parameter (62.62 versus 67.23) is that the sphere may have swelled in the oil medium; the manufacturer states that the particles are National Institutes of Standards and Technology traceable within an aqueous solution. The sensitivity of the observed scattering with respect to perturbations in the input parameters will be reported in a future publication, as will verification of these results at higher numerical aperture.

For large radial distances from the particle center, the discrepancy between prediction and experimental data increases. We suspect that this may be due to the partially coherent nature of the source and are investigating further improvements to the model; these efforts include attempts to model the effect of general rather than plane-wave illumination.[27] In spite of this discrepancy, it is clear that the position of the particle along the optical axis can be recovered from the experimental data. Figure 6 shows that as the scattering is asymmetric with respect to Gaussian best focus, it is also possible to unambiguously determine the direction of the sphere's displacement.

6. CONCLUSIONS

We have developed an optical model to predict the scattering pattern by using Mie scattering theory and image theory. Our model calculates Mie scattering from the particle on the fluid side of the interface, assuming plane-wave illumination. This is typically valid for Köhler illumination in a microscope. It also accounts for refraction of the rays and transmission across the interface. In the next step, the model calculates the propagation of the field from the interface to the entrance pupil of the lens. We model the imaging system as an infinity-corrected, diffraction-limited lens. We do not use a paraxial (parabolic wave-front) approximation for the lens and therefore are able to model imaging with high-NA objectives. Finally, our model calculates the intensity in the image plane by using Fresnel diffraction of the field from the exit pupil of the lens to the image plane of the detector.

APPENDIX A: MIE FIELD

For the purposes of subsequent analysis, in this appendix we describe the scattered Mie field at the interface. The incident and scattered fields are expressed in terms of vector spherical harmonics, which describe the radial and angular dependence of the fields. We list, but do not derive, the Mie scattering amplitudes resulting from incident x-polarized, planar illumination. The interested reader is referred to Ref. 17 for the derivation.

The vector spherical wave functions $\mathbf{M}_{o1l}^{(j)}$ and $\mathbf{N}_{e1l}^{(j)}$ are given with respect to the standard spherical coordinate basis vectors by

$$\mathbf{M}_{o1l}^{(j)}(r,\theta,\phi) = \cos\phi\,\pi_l(\theta) z_l^{(j)}(r)\hat{\mathbf{u}}_\theta - \sin\phi\,\tau_l(\theta) z_l^{(j)}(r)\hat{\mathbf{u}}_\phi, \tag{A1a}$$

$$\mathbf{N}_{e1l}^{(j)}(r,\theta,\phi) = \cos\phi\, l(l+1)\sin\theta\,\pi_l(\theta)\frac{z_l^{(j)}(r)}{r}\hat{\mathbf{u}}_r + \cos\phi\,\tau_l(\theta)\frac{[r z_l^{(j)}(r)]'}{r}\hat{\mathbf{u}}_\theta - \sin\phi\,\pi_l(\theta)\frac{[r z_l^{(j)}(r)]'}{r}\hat{\mathbf{u}}_\phi, \tag{A1b}$$

where the angular functions π_l and τ_l are defined by

$$\pi_l(\theta) = \frac{1}{\sin\theta}P_l^1(\cos\theta), \tag{A2a}$$

$$\tau_l(\theta) = \frac{\mathrm{d}}{\mathrm{d}\theta}P_l^1(\cos\theta). \tag{A2b}$$

P_l^1 denotes the associated Legendre function of the first kind. The superscript (j) selects the appropriate spherical Bessel function $z_l^{(1)}(r) = j_l(r)$ or spherical Hankel function $z_l^{(3)}(r) = h_l^{(1)}(r)$ corresponding to, respectively, standing and outward-traveling waves.

The incident x-polarized, planar wave of amplitude E_0 and wave number k can be expressed in terms of vector spherical wave functions as

$$\mathbf{E}_i(r,\theta,\phi) = E_0\sum_{l=1}^{\infty} E_l[\mathbf{M}_{o1l}^{(1)}(kr,\theta,\phi) - i\mathbf{N}_{e1l}^{(1)}(kr,\theta,\phi)], \tag{A3}$$

where

$$E_l = i^l\frac{2l+1}{l(l+1)}. \tag{A4}$$

The expression for the scattered field is given by[17]

$$\mathbf{E}_s(r,\theta,\phi) = E_0\sum_{l=1}^{\infty} E_l[-b_l\mathbf{M}_{o1l}^{(3)}(kr,\theta,\phi) + ia_l\mathbf{N}_{e1l}^{(3)}(kr,\theta,\phi)], \tag{A5}$$

where the scattering coefficients a_l and b_l are

$$a_l = \frac{n\psi_l(nka)\psi'(ka) - \psi_l(ka)\psi'(nka)}{n\psi_l(nka)\xi'(ka) - \xi_l(ka)\psi'(nka)}, \tag{A6a}$$

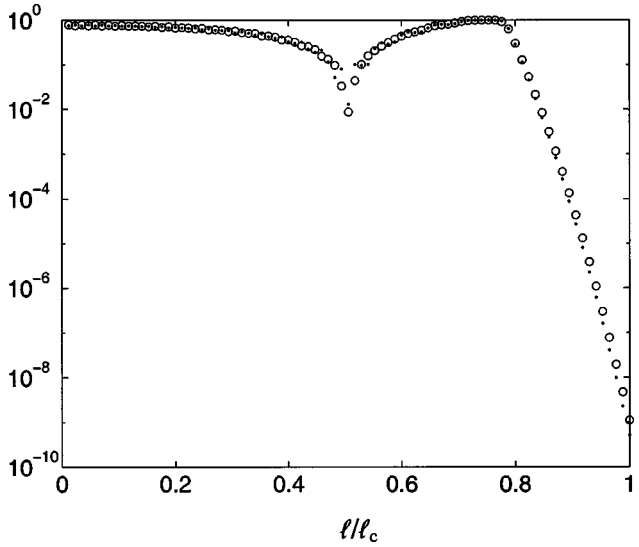

Fig. 7. Log plots for $l_c = 85$ of the coefficients $|a_l|$ (○) and $|b_l|$ (·) for $1 \leqslant l \leqslant l_c$. The coefficients were evaluated by using the experimental parameters.

$$b_l = \frac{\psi_l(nka)\psi'(ka) - n\psi_l(ka)\psi'(nka)}{\psi_l(nka)\xi'(ka) - n\xi_l(ka)\psi'(nka)}. \tag{A6b}$$

ψ_l and ξ_l are the Ricatti–Bessel functions, defined by

$$\psi_l(r) = rj_l(r), \tag{A7a}$$

$$\xi_l(r) = rh_l^{(1)}(r), \tag{A7b}$$

and ka is the size parameter. Finally, $n = n_p/n_f$ is the relative index of refraction between the particle and the fluid.

Equation (A5) must be evaluated for points on the interface. In Ref. 28 it is shown that when $l > ka + 4.3(ka)^{1/3}$, the scattering coefficients a_l and b_l decay very rapidly (Fig. 7), and that for numerical calculation the series can be truncated at $l_c = ka + 4.3(ka)^{1/3}$. Therefore the expression for the scattered field becomes

$$\mathbf{E}_s(r,\theta,\phi) = E_0\sum_{l=1}^{l_c} E_l[-b_l\mathbf{M}_{o1l}^{(3)}(kr,\theta,\phi) + ia_l\mathbf{N}_{e1l}^{(3)}(kr,\theta,\phi)]. \tag{A8}$$

APPENDIX B: FIELD APPROXIMATIONS

Commonly, two far-field approximations are applied to Eq. (A8).[17,19] First, it is assumed that the size of the $\hat{\mathbf{u}}_r$ (radial) component is on the order of $1/(kr)$ times that of the two other transverse components of $\mathbf{E}_s$ and that it can be dropped. Second, it is assumed that kr is sufficiently large such that the spherical Hankel functions appearing in $\mathbf{M}_{o1l}^{(1)}$ and $\mathbf{N}_{e1l}^{(1)}$ can be replaced by decaying complex exponentials. (See Section 4.4.4 of Ref. 17, for example.) We demonstrate that for the parameter values from the experiment, only one of the two approximations, namely, dropping the radial component of $\mathbf{E}_s$, is valid.

To estimate the error in dropping the $\hat{\mathbf{u}}_r$ term, we must compare the relative sizes of the radial and transverse

components in Eq. (A1b). The asymptotic relations for the spherical Hankel functions,[29]

$$h_l^{(1)}(kr) \sim \frac{(-i)^l \exp ikr}{ikr}\left[1 + i\frac{l(l+1)}{2kr}\right], \tag{B1a}$$

$$[h_l^{(1)}]'(kr) \sim \frac{(-i)^l \exp ikr}{kr}\left[1 + i\frac{l(l+1)+1}{2kr}\right], \tag{B1b}$$

show that along any direction (fixed θ and ϕ), the ratio of the magnitude of the radial component to the transverse component behaves like $c(\theta, \phi)/r$ as r gets large. To obtain rigorous bounds on $c(\theta, \phi)$, one must evaluate asymptotic expressions for the functions $\pi_l(\theta)$ and $\tau_l(\theta)$. Rather than follow this complicated analytic approach, we have chosen to numerically verify that the radial component is indeed small with respect to the transverse components. To show this, we computed the ratio of the magnitudes of the radial and transverse components at each point on the fluid side of the interface (Fig. 8). Because the magnitude of the radial component of $\mathbf{E}_s$ is no more than 0.25% of that of the transverse components, its contribution to the Poynting vector is negligible.

With the omission of the radial component, Eqs. (A1) and (A8) together give

$$\begin{aligned}\mathbf{E}_s = E_0 \sum_{l=1}^{l_c} E_l \Bigg\{ & -b_l \pi_l(\theta) h_l^{(1)}(kr) \\ & + i a_l \tau_l(\theta) \frac{[kr h_l^{(1)}(kr)]'}{kr} \Bigg\} \cos\phi\, \hat{\mathbf{u}}_\theta \\ & + E_l \Bigg\{ b_l \tau_l(\theta) h_l^{(1)}(kr) \\ & - i a_l \pi_l(\theta) \frac{[kr h_l^{(1)}(kr)]'}{kr} \Bigg\} \sin\theta\, \hat{\mathbf{u}}_\phi .\end{aligned} \tag{B2}$$

This can be rewritten as Eqs. (8) and (9) with

$$\begin{aligned}S_\parallel(r, \theta) = E_0 \sum_{l=1}^{l_c} E_l \Bigg\{ & -b_l \pi_l(\theta) h_l^{(1)}(kr) \\ & + i a_l \tau_l(\theta) \frac{[kr h_l^{(1)}(kr)]'}{kr} \Bigg\},\end{aligned} \tag{B3a}$$

$$\begin{aligned}S_\perp(r, \theta) = E_0 \sum_{l=1}^{l_c} E_l \Bigg\{ & b_l \pi_l(\theta) h_l^{(1)}(kr) \\ & - i a_l \pi_l(\theta) \frac{[kr h_l^{(1)}(kr)]'}{kr} \Bigg\}.\end{aligned} \tag{B3b}$$

For many experimental realizations of this model, the interface will be too close for the second approximation to be applicable. This common approximation (which is applicable when $kr \gg l^2$) takes only the first term in relations (B1). Because the size of the last term in an asymptotic expansion provides an estimate of the size of the error when the series is truncated just before that term, the validity of the approximation requires that the second term must be small compared with unity. The quantities corresponding to the experiment described in Section 4 are $k = 1.8418 \times 10^7\ \mathrm{m}^{-1}$, $ka \approx 67$, $l_c = 85$, and $z_1 \approx 1.6 \times 10^{-3}$ m. Thus the smallest value kr for the radial argument of the spherical wave functions is $kz_1 \approx 29{,}469$. For this kr the second term in the braces in Eqs. (B1) is approximately $3655/29{,}469 \approx 0.124$. Thus we obtain a worst-case estimate of 12.4% for the error in using only the first term of the asymptotic series in the summands of Eq. (A8). Because the Hankel functions are multiplied by the scattering coefficients, however, the largest error in the summand, attained for $l = 65$, is on the order of 7% (Fig. 9). As a check, if $kr \gg l_c^2$ such that the spherical Hankel functions may be approximated by decaying exponentials, Eqs. (B3) yield the far-field scattering coefficients.

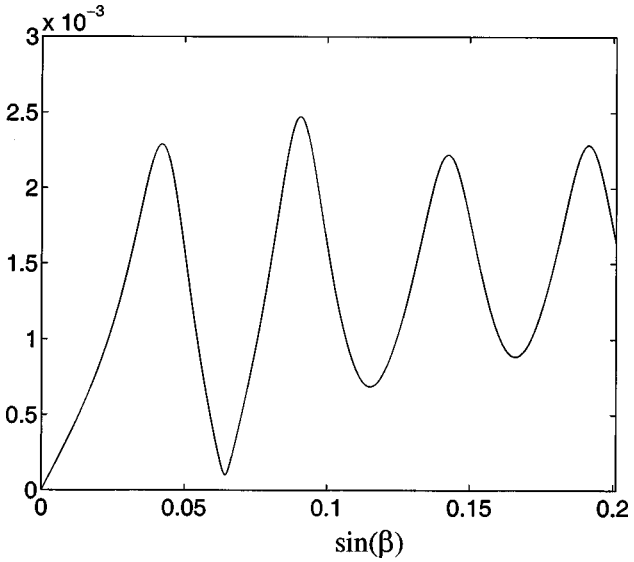

Fig. 8. Ratio of the magnitudes of the radial and transverse components of the scattered field, $\|\mathbf{E}_s \cdot \hat{\mathbf{u}}_r\|/\|\mathbf{E}_s - \mathbf{E}_s \cdot \hat{\mathbf{u}}_r\|$, evaluated at the interface, plotted as a function of $\sin\beta$. The parameters used correspond to experimental values.

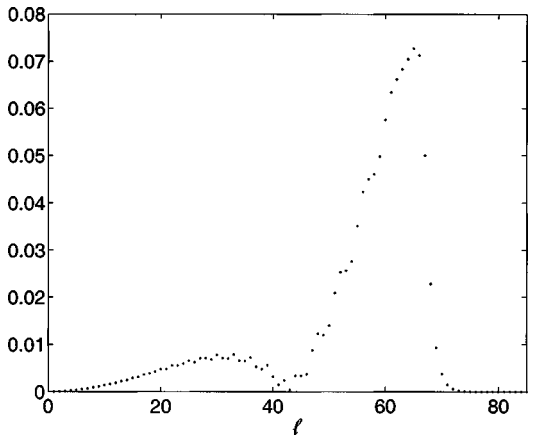

Fig. 9. Relative error in $b_l\,(1 - \{(-i)^l[\exp(ikr)/(ikr)]\}/[h_l^{(1)}(kr)])$ plotted as a function of l at the interface along the optical axis. The parameters used correspond to experimental values.

APPENDIX C: IMAGE FORMATION

In this appendix we will derive the expression for the irradiance at the detector, $I(\rho_4, \alpha)$. In particular, we will

give expressions for the coefficients E_4^0, E_4^1, and E_4^2 that appear in Eq. (32). Because we assumed that the normal to the detector was parallel to the z axis, an evaluation of the Poynting vector is most easily evaluated by expressing all the fields in terms of Cartesian basis vectors.

The coefficients for the incident and scattered fields after propagation to the exit pupil, Eqs. (22) and (28), were expressed in terms of the incident wave. It may be observed that the ϕ dependence appears on the right-hand side of these equations only in $E_{i\|}(\phi)$ and $E_{i\perp}(\phi)$. Therefore these equations are separable in ρ_3 and ϕ. Collecting together in $T_{s\|3}(\rho_3)$, $T_{s\perp 3}(\rho_3)$, $T_{i\|3}(\rho_3)$, and $T_{i\perp 3}(\rho_3)$ the terms from Eqs. (22) and (28) that do not depend on ϕ, we obtain

$$E_{s\|3}(\rho_3, \phi) = T_{s\|3}(\rho_3)\cos\phi, \tag{C1a}$$

$$E_{s\perp 3}(\rho_3, \phi) = -T_{s\perp 3}(\rho_3)\sin\phi, \tag{C1b}$$

$$E_{i\|3}(\rho_3, \phi) = T_{i\|3}(\rho_3)\cos\phi, \tag{C1c}$$

$$E_{i\perp 3}(\rho_3, \phi) = -T_{i\perp 3}(\rho_3)\sin\phi. \tag{C1d}$$

From Eq. (6b),

$$\hat{\mathbf{u}}_{s\|}(\pi - \gamma, \phi) = -\cos\gamma\cos\phi\,\hat{\mathbf{u}}_x + \cos\gamma\sin\phi\,\hat{\mathbf{u}}_y - \sin\gamma\,\hat{\mathbf{u}}_z, \tag{C2a}$$

$$\hat{\mathbf{u}}_{s\perp}(\phi) = -\sin\phi\,\hat{\mathbf{u}}_x + \cos\phi\,\hat{\mathbf{u}}_y, \tag{C2b}$$

where γ represents either γ_i or γ_s. Using the notation of Eqs. (C1) with Eqs. (29), we may express $\mathbf{E}_3$ in terms of the Cartesian basis vectors as

$$\begin{aligned}\mathbf{E}_3(\rho_3, \phi) = {} & \hat{\mathbf{u}}_x\{[-T_{s\|3}(\rho_3)\cos\gamma_s - T_{i\|3}(\rho_3)\cos\gamma_i]\cos^2\phi \\ & + [T_{s\perp 3}(\rho_3) + T_{i\perp 3}(\rho_3)]\sin^2\phi\} \\ & + \hat{\mathbf{u}}_y\{[-T_{s\|3}(\rho_3)\cos\gamma_s \\ & - T_{i\|3}(\rho_3)\cos\gamma_i]\cos\phi\sin\phi \\ & - [T_{s\perp 3}(\rho_3) + T_{i\perp 3}(\rho_3)]\sin\phi\cos\phi\} \\ & + \hat{\mathbf{u}}_z\{[-T_{s\|3}(\rho_3)\sin\gamma_s \\ & - T_{i\|3}(\rho_3)\sin\gamma_i]\cos\phi\}. \end{aligned} \tag{C3}$$

We apply the trigonometric double-angle formulas to obtain

$$\begin{aligned}\mathbf{E}_3(\rho_3, \phi) = {} & \hat{\mathbf{u}}_x\big(\tfrac{1}{2}\{[-T_{s\|3}(\rho_3)\cos\gamma_s - T_{i\|3}(\rho_3)\cos\gamma_i] \\ & + [T_{s\perp 3}(\rho_3) + T_{i\perp 3}(\rho_3)]\} \\ & + \tfrac{1}{2}\{[-T_{s\|3}(\rho_3)\cos\gamma_s - T_{i\|3}(\rho_3)\cos\gamma_i] \\ & - [T_{s\perp 3}(\rho_3) + T_{i\perp 3}(\rho_3)]\}\cos 2\phi\big) \\ & + \hat{\mathbf{u}}_y\big(\tfrac{1}{2}\{[-T_{s\|3}(\rho_3)\cos\gamma_s - T_{i\|3}(\rho_3)\cos\gamma_i] \\ & - [T_{s\perp 3}(\rho_3) + T_{i\perp 3}(\rho_3)]\}\sin 2\phi\big) \\ & + \hat{\mathbf{u}}_z\{[-T_{s\|3}(\rho_3)\sin\gamma_s \\ & - T_{i\|3}(\rho_3)\sin\gamma_i]\cos\phi\}. \end{aligned} \tag{C4}$$

The total field may be expressed by using the compact notation

$$\begin{aligned}\mathbf{E}_3(\rho_3, \phi) = {} & [E_3^0(\rho_3) + E_3^2(\rho_3)\cos 2\phi]\hat{\mathbf{u}}_x \\ & + [E_3^2(\rho_3)\sin 2\phi]\hat{\mathbf{u}}_y + [E_3^1(\rho_3)\cos\phi]\hat{\mathbf{u}}_z, \end{aligned} \tag{C5a}$$

where

$$E_3^0(\rho_3) = \tfrac{1}{2}\{[-T_{s\|3}(\rho_3)\cos\gamma_s - T_{i\|3}(\rho_3)\cos\gamma_i] + [T_{s\perp 3}(\rho_3) + T_{i\perp 3}(\rho_3)]\}, \tag{C5b}$$

$$E_3^1(\rho_3) = -T_{s\|3}(\rho_3)\sin\gamma_s - T_{i\|3}(\rho_3)\sin\gamma_i, \tag{C5c}$$

$$E_3^2(\rho_3) = \tfrac{1}{2}\{[-T_{s\|3}(\rho_3)\cos\gamma_s - T_{i\|3}(\rho_3)\cos\gamma_i] - [T_{s\perp 3}(\rho_3) + T_{i\perp 3}(\rho_3)]\}. \tag{C5d}$$

As a result of the simple form of the ϕ dependence of Eqs. (C5), the inner integral of Eq. (30) can be determined analytically by using[29]

$$J_p(\rho) = \frac{i^{-p}}{\pi}\int_0^{\pi}\exp(i\rho\cos\phi)\cos p\phi\,\mathrm{d}\phi. \tag{C6}$$

Therefore Eq. (30) reduces to the compact form

$$\begin{aligned}\mathbf{E}_4(\rho_4, \alpha) = {} & [E_4^0(\rho_4) + E_4^2(\rho_4)\cos 2\alpha]\hat{\mathbf{u}}_x \\ & + [E_4^2(\rho_4)\sin 2\alpha]\hat{\mathbf{u}}_y + [E_4^1(\rho_4)\cos\alpha]\hat{\mathbf{u}}_z, \end{aligned} \tag{C7a}$$

where the coefficients $E_4^p(\rho_4)$, for $p = 0,1,2$, are given by

$$\begin{aligned}E_4^p(\rho_4) = {} & i^p\frac{\pi}{\lambda z_4}\exp\left(\frac{\pi i}{\lambda z_4}{\rho_4}^2\right)\int_0^A W_\mu(\rho_3) \\ & \times\exp\left(\frac{\pi i}{\lambda z_4}{\rho_3}^2\right)J_p\left(\frac{\pi\rho_4\rho_3}{\lambda z_4}\right)E_3^p(\rho_3)\rho_3\mathrm{d}\rho_3. \end{aligned} \tag{C7b}$$

Because the detector at the image plane is oriented normally to the optical axis, a determination of the Poynting vector at the image plane does not require a computation of the $\hat{\mathbf{u}}_z$ component; it is included, however, for completeness. Therefore the irradiance is

$$I(\rho_4, \alpha) = |E_{4x}|^2 + |E_{4y}|^2 \tag{C8}$$

$$= |E_4^0(\rho_4) + E_4^2(\rho_4)\cos 2\alpha|^2 + |E_4^2(\rho_4)\sin 2\alpha|^2 \tag{C9}$$

$$= |E_4^0(\rho_4)|^2 + |E_4^2(\rho_4)|^2 + 2\,\mathrm{Re}\{E_4^0(\rho_4)[E_4^2(\rho_4)]^*\}\cos 2\alpha. \tag{C10}$$

ACKNOWLEDGMENTS

This work was funded by the Microgravity Science Division at the NASA–Glenn Research Center. S. H. Izen was supported by NASA-American Society for Engineering Education summer faculty fellowships. Our Mie calculations were based upon a modified version of code initially written by J. A. Lock (Cleveland State University). We acknowledge the significant contributions of J. D.

Khaydarov (Continuum, Inc.) to both experimental data collection and model formulation (J. D. Khaydarov was a resident research associate under the auspices of the Ohio Aerospace Institute).

Address correspondence to Ben Ovryn, NASA-Glenn Research Center, MS 110-3, 21000 Brookpark Road, Cleveland, Ohio 44135-3127, or by e-mail, bxo3@po.cwru.edu.

REFERENCES

1. C. J. R. Sheppard and T. Wilson, "The image of a single point in microscopes of large numerical aperture," Proc. R. Soc. London Ser. A **379**, 145–158 (1982).
2. C. J. R. Sheppard and H. J. Matthews, "Imaging in high-aperture optical systems," J. Opt. Soc. Am. A **4**, 1354–1360 (1987).
3. T. R. Corle and G. S. Kino, *Confocal Scanning Optical Microscopes and Related Imaging Systems* (Academic, New York, 1996).
4. P. Török and T. Wilson, "Rigorous theory of axial resolution in confocal microscopes," Opt. Commun. **137**, 127–135 (1997).
5. T. Wilson, R. Juskaitis, and P. Higdon, "The imaging of dielectric point scatterers in conventional and confocal polarization microscopy," Opt. Commun. **141**, 298–313 (1997).
6. J. C. Crocker and D. G. Grier, "Methods of digital video microscopy for colloidal studies," J. Colloid Interface Sci. **179**, 298–310 (1996).
7. T. G. Mason, J. H. van Zanten, and D. Wirtz, "Particle tracking microrheology of complex fluids," Phys. Rev. Lett. **79**, 3282–3285 (1997).
8. M. Hammer, D. Schweitzer, B. Michel, E. Thamm, and A. Kolb, "Single scattering by red blood cells," Appl. Opt. **37**, 7410–7418 (1998).
9. S. A. Schaub, D. R. Alexander, and J. P. Barton, "Theoretical model of the laser imaging of small aerosols: applications to aerosol sizing," Appl. Opt. **30**, 4777–4784 (1991).
10. M. D. Barnes, N. Lerner, W. B. Whitten, and J. M. Ramsey, "A CCD based approach to high-precision size and refractive index determination of levitated microdroplets using Fraunhofer diffraction," Rev. Sci. Instrum. **68**, 2287–2290 (1997).
11. W. Weise, P. Zinin, T. Wilson, A. Briggs, and S. Boseck, "Imaging of spheres with the confocal scanning optical microscope," Opt. Lett. **21**, 1800–1802 (1996).
12. Y. Hiraoka, J. W. Sedat, and D. A. Agard, "Determination of three-dimensional imaging properties of a light microscope system," Biophys. J. **57**, 325–333 (1990).
13. B. Richards and E. Wolf, "Electromagnetic diffraction in optical systems. II. Structure of the image field in an aplanatic system," Proc. R. Soc. London, Ser. A **253**, 358–379 (1959).
14. R. Kant, "An analytical solution of vector diffraction for focusing optical systems," J. Mod. Opt. **40**, 337–347 (1993).
15. P. Török, S. J. Hewlett, and P. Varga, "On the series expansion of high-aperture, vectorial diffraction integrals," J. Mod. Opt. **44**, 493–503 (1997).
16. B. Ovryn and J. D. Khaydarov, "Forward scattering particle image velocimetry (FSPIV): application of Mie and imaging theory to measure 3D velocities in microscopic flows using partially coherent illumination and high aperture optics," in *Three-Dimensional Microscopy: Image Acquisition and Processing IV*, C. J. Cogswell, J. Conchello, and T. Wilson, eds., Proc. SPIE **2984**, 243–254 (1997).
17. C. F. Bohren and D. R. Huffman, *Absorption and Scattering of Light by Small Particles* (Wiley, New York, 1983).
18. J. A. Stratton, *Electromagnetic Theory* (McGraw-Hill, New York, 1941).
19. H. C. van de Hulst, *Light Scattering by Small Particles* (Dover, New York, 1981).
20. L. Mandel and E. Wolf, *Optical Coherence and Quantum Optics* (Cambridge U. Press, New York, 1995).
21. M. Born and E. Wolf, *Principles of Optics*, 6th ed. (Pergamon, New York, 1980).
22. D. G. Flagello, T. Milster, and A. E. Rosenbluth, "Theory of high-NA imaging in homogeneous thin films," J. Opt. Soc. Am. A **13**, 53–64 (1996).
23. M. Mansuripur, "Certain computational aspects of vector diffraction problems," J. Opt. Soc. Am. A **6**, 786–805 (1989).
24. H. Osterberg and J. E. Wilkins, "The resolving power of a coated objective," J. Opt. Soc. Am. **39**, 553–557 (1949).
25. J. Goodman, *Introduction to Fourier Optics* (McGraw-Hill, New York, 1968).
26. M. Mansuripur, "Distribution of light at and near the focus of high-numerical-aperture objectives," J. Opt. Soc. Am. A **3**, 2086–2093 (1986).
27. S. H. Izen and B. Ovryn, "Imaging spheres with general incident wavefronts using a dipole decomposition," in *Three-Dimensional and Multidimensional Microscopy: Image Acquisition and Processing V*, C. J. Cogswell, J. Conchello, T. Wilson, T. T. Lu, and J. M. Lerner, eds., Proc. SPIE **3261**, 7–16 (1998).
28. W. J. Wiscombe, "Improved Mie scattering algorithms," Appl. Opt. **19**, 1505–1509 (1980).
29. M. Abramowitz and I. Stegun, *Handbook of Mathematical Functions* (Dover, New York, 1964).